Resolution power of Gaia

A comparison of the interferometer and the mono-pupil telescope options for resolving asteroids.

Daniel Hestroffer
OATO, Italy

October 15, 1998

Abstract

This notes compares the resolution power achievable by the monolithic telescope and the binocular interferometer options. Preliminary numbers of resolved asteroids are given from either the IRAS IR-survey data-base, or from a more extensive data-base of known asteroids. The 2.45 m interferometer would have a slightly higher resolution power than the 1.7×0.7 m monolithic telescope; in terms of number of resolved objects the interferometer would however resolve approximately 50% more asteroids than the monolithic telescope. Both options would provide diameters of asteroids for comparison to the IRAS results.

1 Introduction

We study the ability to resolve asteroids with Gaia; resolution of stars is briefly examined for the moment but the code already includes different stellar spectral responses and can be extended to comets. In a first approximation these celestial bodies can be assumed to be spherical for this purpose; effects of flattened disks and solar phase angle can be regarded as a small departure from this ideal case. Effects of the TDI mode (or drift-scan mode) and sampling by the CCD as well as effects due to the motion of asteroids and limb-darkening are taken into account. We consider two technical solutions proposed either by Matra Marconi Space (MMS) or by Alenia Spazio (ALS), solutions which consist in a monolithic pupil for MMS or an interferometer for ALS. In a way similar to the visibility function for an interferometer, we quantify the departure from the PSF for a non point-like source. The limit of resolution – defined on a statistical basis – in both cases is compared and given in terms of number of asteroids that could be resolved. It appears that the interferometer and the monolithic telescope would yield similar resolution power, and could resolve asteroids with angular diameters larger than 15 – 20 mas depending on their actual brightness.

2 Asteroid modeling

The larger fraction of known asteroids lies in the range going from 2 to 3.5 AU, which consists essentially of S-type asteroids with moderate albedo (40% of the asteroidal population at 2.3 AU) and C-type asteroids with very low albedo (80% at 3.2 AU), M-type can be considered to constitute the rest of the population (10% at 2.7 AU). The spectrum has been modeled for either a typical C-type or S-type asteroid. Reflectance normalized at 550 nm from the SMASS survey (Xu et al. 1995) were multiplied by a T=6500 K solar spectrum. Normalization at 550 nm ensures that the V magnitudes of the two objects are close enough for this study. The variation of the PSFs between the C and S asteroids spectral type is small; also the intensity distribution for both options is close to the PSF of a G2V star with no absorption.

The limb-darkening of a spherical asteroid is modeled by Minnaert's law of single real parameter $1/2 \leq k \leq 1$ assuming there is no phase ($\alpha = 0$). The centre-normalized brightness distribution across the surface is then given by:

$$I = \mu^{2\,k-1} = (1 - u^2)^{k-1/2} + o\,(\alpha) \tag{1}$$

where u is the normalized distance from the center. This yields a uniformly bright disk for $k = 1/2$ and a Lambertian disk for $k = 1$. Ellipsoidal shape (flattened disk) and solar phase angle are also implemented in the code. The 'flattening' coefficient $0 < \zeta$ is defined here as the ratio of the cross-scan length over the along-scan length for an apparent ellipse which principal axes are parallel to these cross- and along-scan directions.

The apparent magnitude V is calculated at quadrature by assuming circular orbits (see Sect. A.3) and from the knowledge of the IAU (H, G) system:

$$V = H + 5\,\log(r\sqrt{r^2 - 1}) - 2.5\log\Big((1 - G)\,\phi_1(\alpha) + G\,\phi_2(\alpha)\Big) \tag{2}$$

where r is the distance from the asteroid to the sun (or the semi-major axis for a circular orbit). A mean apparent diameter is calculated for an asteroid at the quadrature by adopting the following relation:

$$D = \sqrt{\frac{2}{p_{\rm V}}}\; a\; 10^{-0.2\,(H - m_{\odot})} \sim \frac{1338.5}{\sqrt{p_{\rm V}}}\; 10^{-0.2\,H}\ \text{(in km)} \tag{3}$$

where D is the linear diameter, $p_{\rm V}$ is the visual albedo, a the astronomical unit, H the asteroid's absolute magnitude and $m_{\odot} = -26$, the magnitude of the sun at the distance of one astronomical unit. This diameter-magnitude relation depends on the albedo, which in turn is generally unknown. Moreover the albedo uncertainty ($\Delta p/p$) for a given taxonomic class is estimated to be less than 50%, which contributes to a diameter uncertainty ($\Delta D/D$) of 25%.

3 Interferometer

The characteristics retained for the interferometer are summarized in Table 1. The PSF for a point-like source, was calculated with a narrow-band exponential filter for a G2 star, a C-type and S-type asteroid from:

$$I_*^{\mathrm{B}}(x,y) = 4 \int_\lambda \mathrm{G}(\lambda)\, F(\lambda)\, S(\lambda)\, \cos^2(\pi\, x\, B/\lambda) \left[\frac{J_1(\pi\, r\, D/\lambda)}{\pi\, r\, D/\lambda}\right]^2 d\lambda \tag{4}$$

where $r = (x^2+y^2)^{1/2}$, $\mathrm{Q}(\lambda)$ is the MMS#1 moderate CCD quantum efficiency, and $S(\lambda)$ is the spectrum of the object yielding a $V = 15$ magnitude. The integration is done over a 200 nm FWMH exponential filter $F(\lambda)$ centered at $\lambda_o = 750$ nm, taking into account an optical transmittance of .9 and a reference Strehl ratio of .8 at 550 nm.

Table 1: *Characteristics of the interferometer.*

Baseline	B	2.45 m
Aperture (2)	D	0.65 m
Focal length	f	40 m
Wavelength	λ	750 nm
Passband	$\Delta\lambda$ ($\Delta\lambda/\lambda$)	200 (0.267)
CCD QE	$\mathrm{G}(\lambda)$	.65 at 660 nm
Pixel size		$4 \times 50\,\mu$m
Limiting magnitude		$V < 19$

For an extended source of apparent diameter ϕ, the intensity distribution is given by:

$$I^{\mathrm{B}}(x,y) = \Big(\pi\zeta(1+\cos\alpha)/(2k+1)\Big)^{-1} \int_u \int_v (1-u^2-v^2)^{k-1/2}\, I_*^{\mathrm{B}}(x-u, y-v)\, du\, dv \tag{5}$$

where ζ, α and k are the flattening coefficient, the solar phase angle and the limb-darkening coefficient respectively. The integration steps are adapted for diameters up to $5.243\,\lambda/B$, yielding an accuracy of 10^{-3} for the difference $I^{\mathrm{B}}(x,0) - I_*^{\mathrm{B}}(x,0)$, but not for the function $I^{\mathrm{B}}(x,y)$ itself. The contrast of the fringes disappears for an apparent diameter of $\phi \simeq 1.22\,\lambda_o/B \simeq 76.9$ mas.

4 Mono-pupil

The characteristics retained for the monolithic telescope are summarized in Table 2. The PSF was calculated by:

$$I_*^{\mathrm{M}}(x,y) = \int_\lambda \mathrm{G}(\lambda)\, S(\lambda)\, \mathrm{sinc}^2\,(x\, a/\lambda)\, \mathrm{sinc}^2\,(y\, b/\lambda)\; d\lambda \tag{6}$$

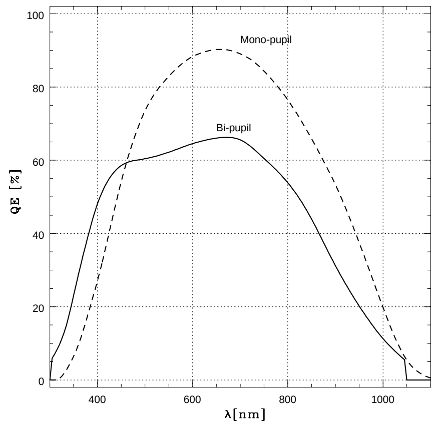

Figure 1: *Quantum efficiency* (QE) *of the* CCDs *retained in this study for the monolithic telescope and the interferometer.*

where G(λ) is the MMS#3 high CCD quantum efficiency given in Mignard (1998a) over the passband $\lambda \in [300; 1\,200]$ nm and $S(\lambda)$ is the spectrum of the object. There is no additional filter here. A comparison of the CCDs QEs is given in Fig. 1.

Table 2: *Characteristics of the monolithic telescope.*

Pupil	$a \times b$	1.7×0.7 m
Focal length	f	50 m
Passband	$\Delta\lambda$	300 – 1 200 nm
CCD QE	G(λ)	.9 at 660 nm
Pixel size		$9 \times 27\,\mu$m
Limiting magnitude		$V < 20$

Similarly to Eq. (5), the intensity distribution for an extended source is given by:

$$I^{\mathrm{M}}(x,y) = \Big(\pi\zeta(1{+}\cos\alpha)/(2k{+}1)\Big)^{-1} \int_u \int_v (1{-}u^2{-}v^2)^{k-1/2}\, I_*^{\mathrm{M}}(x{-}u, y{-}v)\, du\, dv \tag{7}$$

5 Visibility

An object being resolved with an interferometer when the visibility – or contrast – of the fringes is significantly reduced:

$$\mathcal{V} = \frac{I_{\max} - I_{\min}}{I_{\max} + I_{\min}} < 1\,, \tag{8}$$

we compare the resolution of both kinds of instruments from the departure of the normalized intensity distribution to the modeled PSF for a point-like source. Different approach were considered either on the sampled PSF or its Fourier transform. They yield similar results for the resolution power. For the mono-pupil telescope an exponential fit to the PSF yields its FWMH, while for the interferometer we derived a non-linear fit of the form:

$$\begin{aligned} X &= x - A_6 \\ f(X) &= A_0 + A_1 \exp(-\frac{X^2}{2\,A_2^2}) + \\ & \qquad A_3 \exp(-\frac{X^2}{2\,A_4^2}) \cos(2\,\pi\,X/A_5) \end{aligned} \tag{9}$$

where A_5 is the known fringe period. The fringes' contrast in this case is derived from Eq. (8). This fit is adapted for diameters ranging from 0 to 110 mas and objects fainter than $V < 19$. Nevertheless initial values have to be given to the free parameters; to ensure the convergence of the process, these differ whether the object is larger or smaller than $\phi \approx 40$ mas. Moreover the position of the central extremum (or axis of symmetry of the PSF) has to be known to within one pixel[1]. This can be given for instance from the location estimator yielding the astrometry. In this study the known offset of the CCD was taken as an input parameter. Moreover, we determine for both instruments the total energy of the normalized PSF (FFT1), or the value of its Fourier transform $\widehat{\text{PSF}}$ at a given point (FFT2) (see Fig. 2).

As shown in Fig. 3, the visibility function for the interferometer of a uniformly bright disk of angular diameter $\phi \lesssim \lambda/B$ can adequately be given by:

$$\mathcal{V}(x) = 2\,\frac{|J_1(x)|}{x} = |\,{}_0F_1(2; -x^2/4)\,|, \quad \text{with } x = \pi\phi\,B/\lambda \tag{10}$$

where J_1 and ${}_0F_1$ are the Bessel and the hypergeometric function respectively, and $\lambda = 750$ nm. The discrepancy is due to the model used for the calculation of the visibility (here FFT2); the code should be improved to limit bias effects. The FWMH for the monolithic telescope of a uniformly bright disk can be given by:

$$\text{FWMH} = 1.772 + 7.5\,10^{-5}\,\phi^2 \quad ; \quad \text{S-type} \tag{11}$$

$$\text{FWMH} = 1.738 + 7.5\,10^{-5}\,\phi^2 \quad ; \quad \text{C-type} \tag{12}$$

where the angular diameter ϕ is expressed in mas. Similarly the (FFT2) visibility of a C-type asteroid can be fitted by:

$$\mathcal{V} = 1 - 3.9\,10^{-5}\,\phi^2 \tag{13}$$

For sake of brevity and for both options, we call visibility the value of these estimators normalized to unity for a point-like source.

[1]This condition is not necessary but when fulfilled, it avoids further test on the χ^2 minimization to distinguish the central extremum from the neighboring ones.

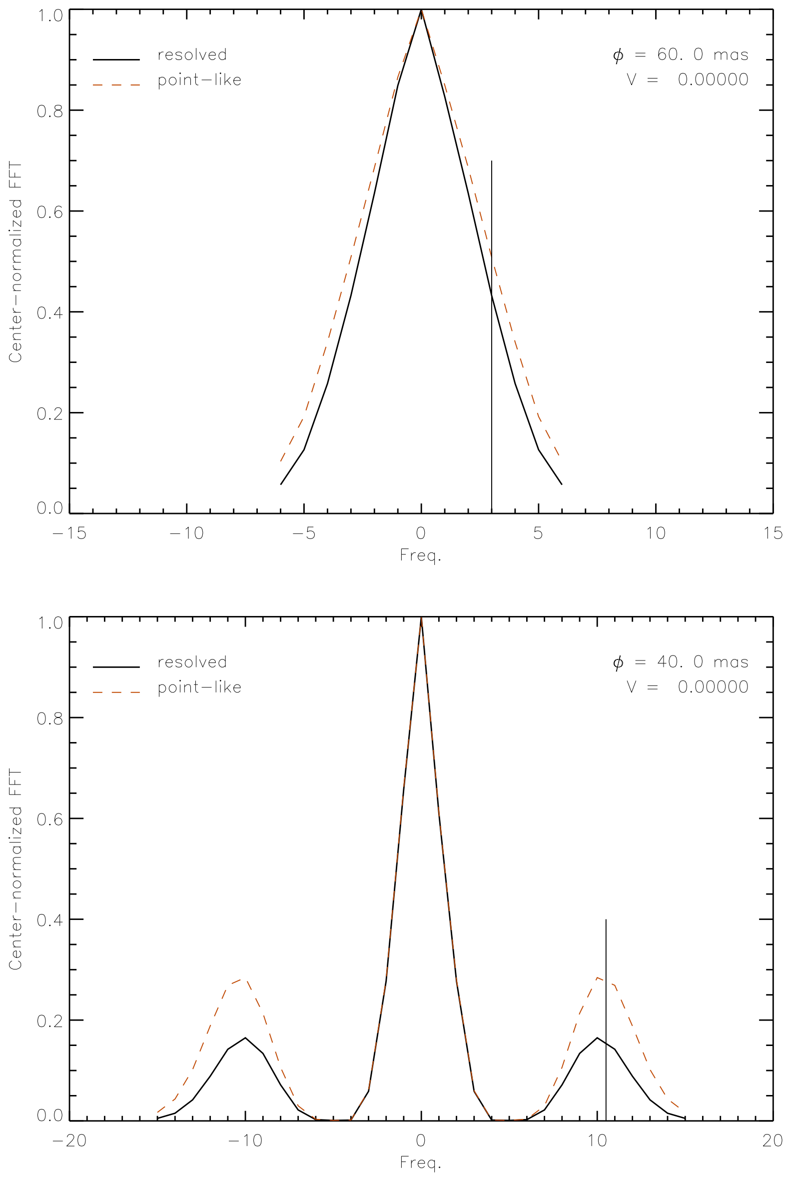

Figure 2: *Fourier transform of the* PSF *and the image of a resolved object with the mono-pupil (top) and the bi-pupil (bottom) telescopes. The frequencies used to quantify the departure from a point-like source are also shown for the FFT2 estimator. Graphs are given for noiseless signals* ($V = 0$).

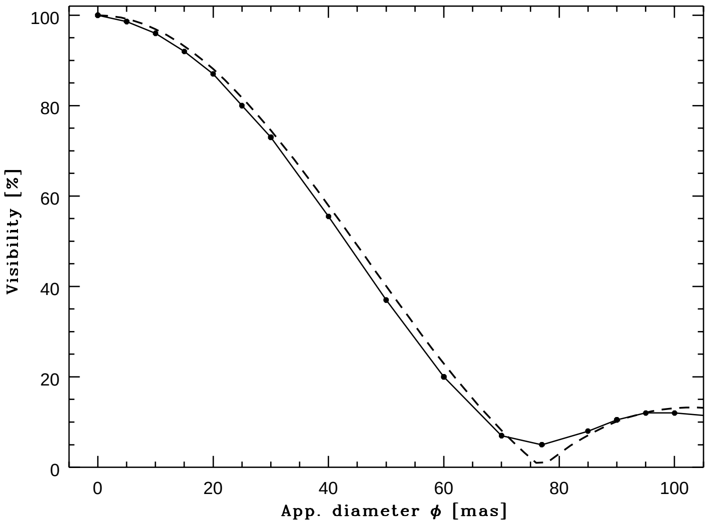

Figure 3: *Visibility for the interferometer as a function of the apparent diameter (FFT2 solution). The dashed curve is the theoretical function of Eq. (10).*

6 CCD number of phases

In a previous version of the code (Mignard, 1998b) the number of the phases of the CCD was not taken into account. This corresponds to a mono-phase CCD. With a larger number of electrodes, typically three, the follow-up of the moving pattern is better matched, thus the visibility or 'focus' is enhanced. In a first approximation we can consider that the convolution from the TDI mode is done with a pixel of size three times smaller, with an appropriate scaling of the intensity for the actual pixel size . Considering a 3-phased CCD has little effect on the precision of the visibility measurements and resolution power, but on the value of the visibility itself.

7 Resolution power

Simulation were performed to determine the variation with magnitudeof the different visibilities' estimators precisions. We find a general relation – valid for objects fainter than $V \gtrsim 10$ – of the form:

$$\log \sigma_{\mathcal{V}}(V) = A + B\,V \tag{14}$$

were the values of the parameters – for a point-like source – are given in Table 3. Variation with apparent size are small although systematic, they are neglected in the following.

Table 3: *Parameters for estimation of the precision of the visibility in Eq. (14).*

visibility definition	A	B
mono-pupil		
FWMH	-3.8	.143
FFT1	-4.3	.158
FFT2	-5.1	.199
bi-pupil		
Contrast	-5.0	.217
FFT1	-4.4	.192
FFT2	-4.4	.196

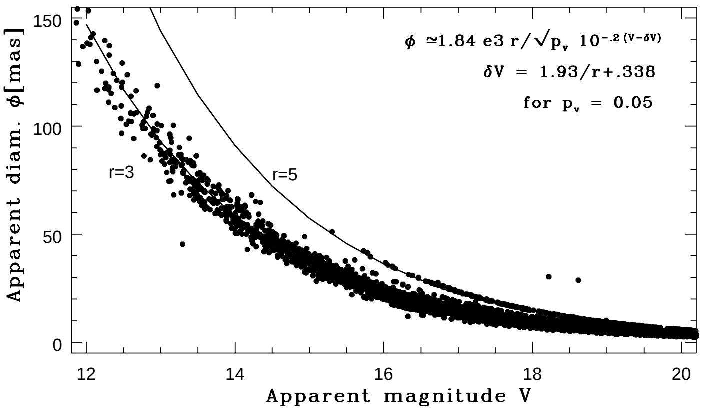

Figure 4: *Magnitude size relation at* $p_{\rm v} = 0.05$.

Next simulations were performed to determine the variation of the value of the visibility with the apparent size of the asteroid. For a typical main-belt or Trojan asteroid, the apparent size ϕ and apparent magnitude V at quadrature can be related with sufficient accuracy by (see Fig. 4):

$$\phi\ [\mathrm{mas}] \approx 1.838\, 10^3/\sqrt{p_{\rm v}}\, r\ 10^{-0.2\,(V-\delta V)} \qquad (15)$$

where r is the heliocentric distance, $p_{\rm v}$ the visual albedo, and $\delta V \sim 1.93/r + 0.338$ the corrective term due to the solar phase (the latter approximation is not valid for $r \gtrsim 6$ or $r \lesssim 1.5$). This yields the $3\,\sigma$ threshold for the resolution of an asteroid given in Fig. 5. Thus we define the resolution power on a statistical basis, i.e. $P(\phi > 0) = 0.999$. With a mono-phase CCD, it appears that both options show roughly the same resolution power. With a 3-phase CCD, the resolution power depends on the solution used to quantify the 'visibility' and is higher for the bi-pupil option. There is a strong correlation between the value of the various estimators and the phase offset of the pixel wrt the continous PSF. This affects mainly the observations of bright object. Making use of the fit given in Eq. (9) generally yields better results for the precision, but the bias is higher. Improvements will be undertaken in further analysis. Hence determination based on the Fourier transform were prefered at this stage. Results on the visibility precision for the interferometer are in very good agreement with those of Gai et al. (1998b) for objects brighter than $V < 16$; for fainter objects the difference is still acceptable but the FFT2 estimator used in the present work yields more optimistic results. Moreover it is stressed that the accuracies of the different estimators are not discussed here.

Over a single CCD crossing, a dark main-belt asteroid ($p_{\mathrm{v}} = .05$) larger than 23 mas could be resolved with the interferometer, while brighter ones ($p_{\mathrm{v}} = .19$) can be resolved at the $3\,\sigma$ level at 18 mas (see Fig. 5). On the other hand, with the mono-pupil telescope dark main-belt objects larger than 28 mas could be resolved, while brighter ones can be resolved at 23 mas. Smaller objects could still be resolved by combining the observations gathered over the whole transit accross the field of view, or eventually two successive transits as shown in Fig. 6. Assuming that for both options 20 CCDs chips will collect the same image, the limit of resolution of an asteroid is significantly enhanced to approximately 14 mas for the interferometer, and 17 mas for the monolithic option ($p_{\mathrm{v}} = .05$). These correspond to a 20–25 km size main-belt asteroid as shown in Fig. 7. The number of potentially resolved asteroids is discussed in Sect. 10.

8 Effects of limb-darkening and motion

The small bodies of the solar system are not uniformly bright but slightly limb-darkened. For a given apparent size, the higher the limb-darkening, the higher the visibility of the fringes, or the smaller the FWMH for the mono-pupil PSF. Actually less objects will be partially resolved. To provide a more realistic number of resolved objects, we consider an empirical limb-darkening following Minnaert's law of parameter $k(\alpha, \lambda) = k$. Neglecting phase effect at this stage, the visibility function now writes (Hestroffer 1997):

$$\mathcal{V}_k(x) = |\,{}_0F_1(k + 3/2; -x^2/4)\,| \tag{16}$$

Putting $k = 0.65$, this yields a slightly larger equivalent apparent diameter ϕ_{UD} with a 1.05 ratio. In the extreme case of a Lambertian disk ($k = 1$), the ratio is of 1.17. On the other hand, the motion of a typical main-belt asteroid can be of the order of 10–15 mas/s. This motion is implemented in the code as an along-scan motion (Mignard, 1998b). Its effect is to diminish the visibility or enlarge the FWMH of the mono-pupil PSF. Limb darkening and motion have effects of opposite value and of approximately similar size (see Table 4 and Fig. 8). Assuming a Minnaert parameter of $k = 0.65$, they compensate

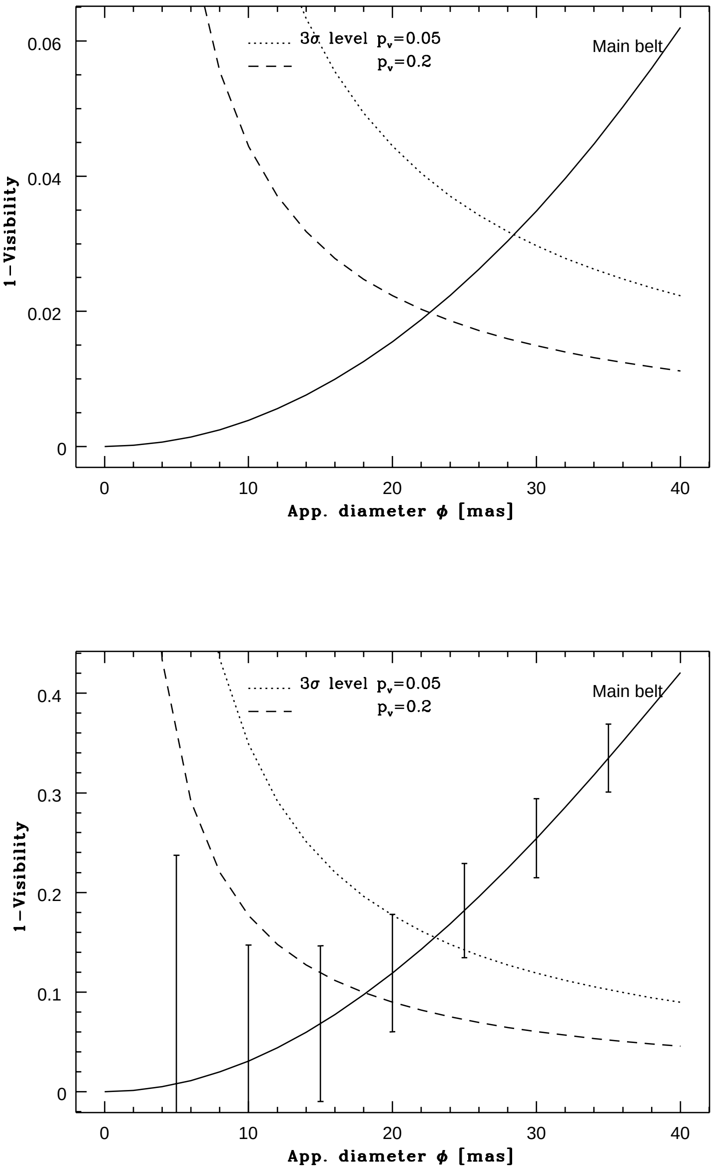

Figure 5: *Resolution power – for a main-belt asteroid at 3* AU *– over a single* CCD *transit for the monolithic (upper panel) and bi-pupil telescopes (lower panel). Error bars are reminded for a* $p_{\rm v} = .05$ *asteroid.*

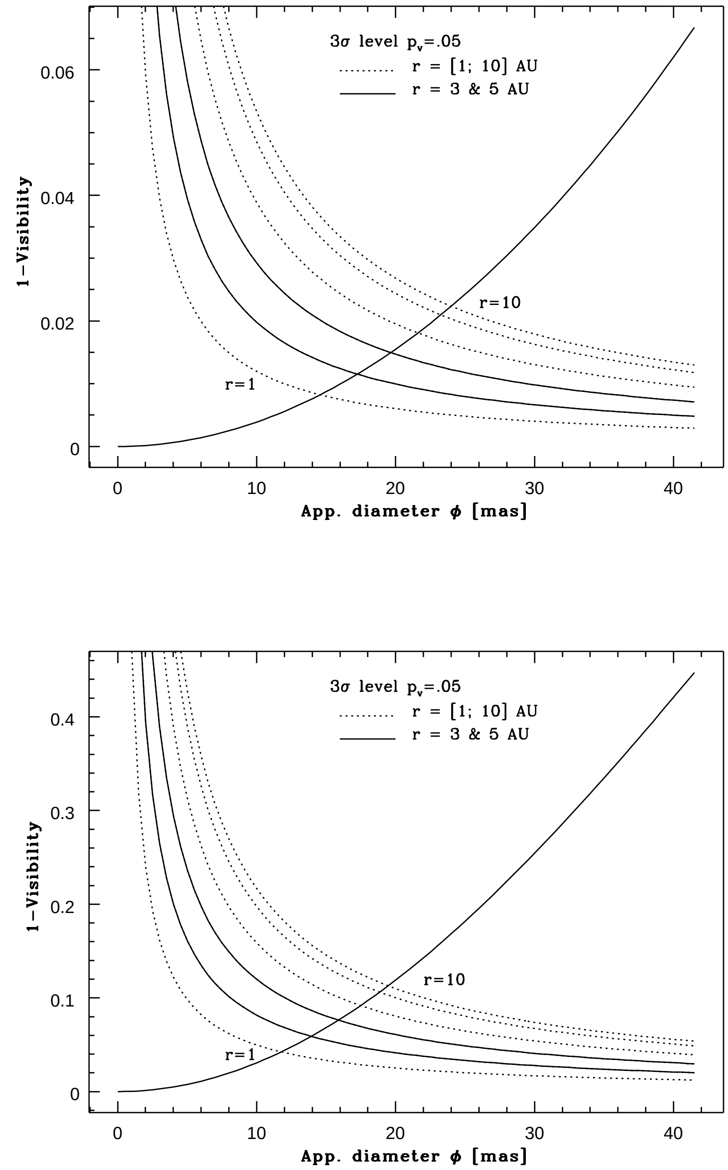

Figure 6: *Resolution power for various heliocentric distance over a* FOV *transit for the monolithic (upper panel) and bi-pupil telescopes (lower panel). All curves are given for a* $p_{\rm v} = .05$ *asteroid.*

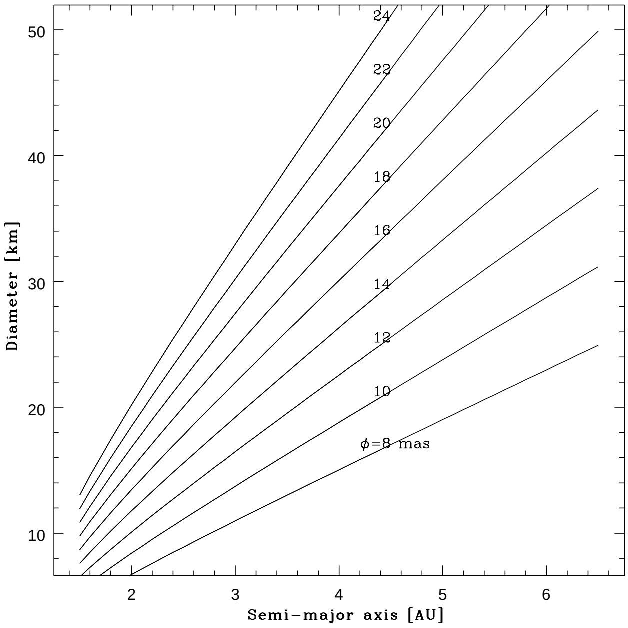

Figure 7: *Size of resolved objects versus semi-major axis.*

for a 25 mas large asteroid with a positive velocity of $v = 10$ mas/s, and for a 50 mas large asteroid with a positive velocity of $v = 20$ mas/s. As long as the relative motion of the asteroid is not compensated by a proper clocking of the CCD, its effect has to be taken into account a posteriori for the derivation of the true diameter of the source.

Table 4: *Visibility $\mathcal{V}$ in percent as a function of the limb-darkening parameter k and the along-scan velocity v of an asteroid.*

k	.5	.65	.8	1
$\phi = 0$	–	–	–	–
$\phi = 25$ mas	81	82	83	85
$\phi = 50$	41	44	47	51
v [mas/s]	0	10	15	20
$\phi = 0$	100	98	96	93
$\phi = 25$	81	80	78	76
$\phi = 50$	41	40	39	38

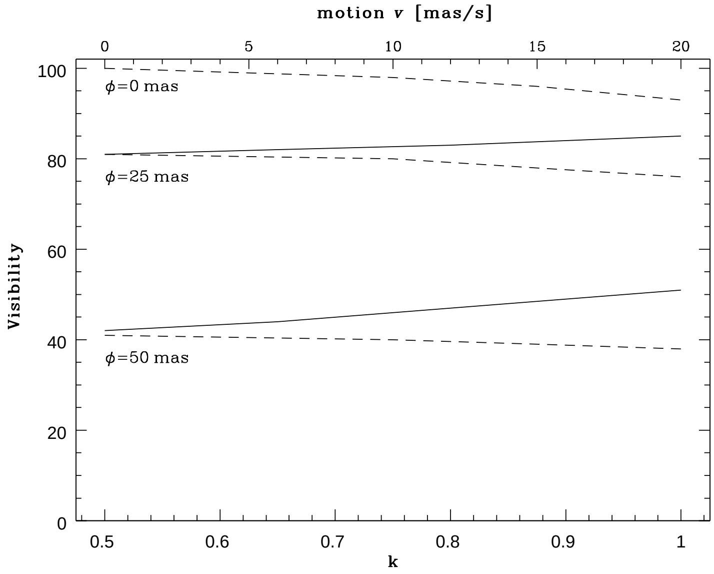

Figure 8: *Variation of the visibility $\mathcal{V}$ with the limb-darkening parameter k (solid line) and the along-scan velocity v (dashed curve) of an asteroid.*

9 Number of detected asteroids

Will shall first consider the 2004 asteroids whose IR diameter is known, by the Infra-Red Flux Method, from the IRAS survey (Tedesco 1989). This diameter determination is model dependent and did necessitate calibration from diameters measurements obtained in the visible. The 1957 IRAS numbered objects external to the earth orbit are in general bright enough to be detected by both instruments.

Next we consider the objects cataloged in the `astorb.dat` data-base of Bowell et al. (1994, up-dated version of June 1998). It is stressed that due to the limiting magnitude of ground-based observations, or bias due to surveys near the ecliptic, this catalogue is not complete up to magnitude $V \sim 20$. We only keep objects whose semi-major axis is larger than 1 AU, hence 30 objects were excluded (see Sect. A.2). Over the 39 700 asteroids contained in the data base, 25 800 would be brighter than $V < 20$ at quadrature, and 15 500 brighter than $V < 19$. These objects are essentially main-belt asteroids, although an appreciable number of Trojans of Jupiter and a couple of Centaurs would also be detected (see Fig. 9). The cumulative numbers of asteroids brighter than $V = 20$, as a function of apparent size are given in Fig. 10 and Fig. 11.

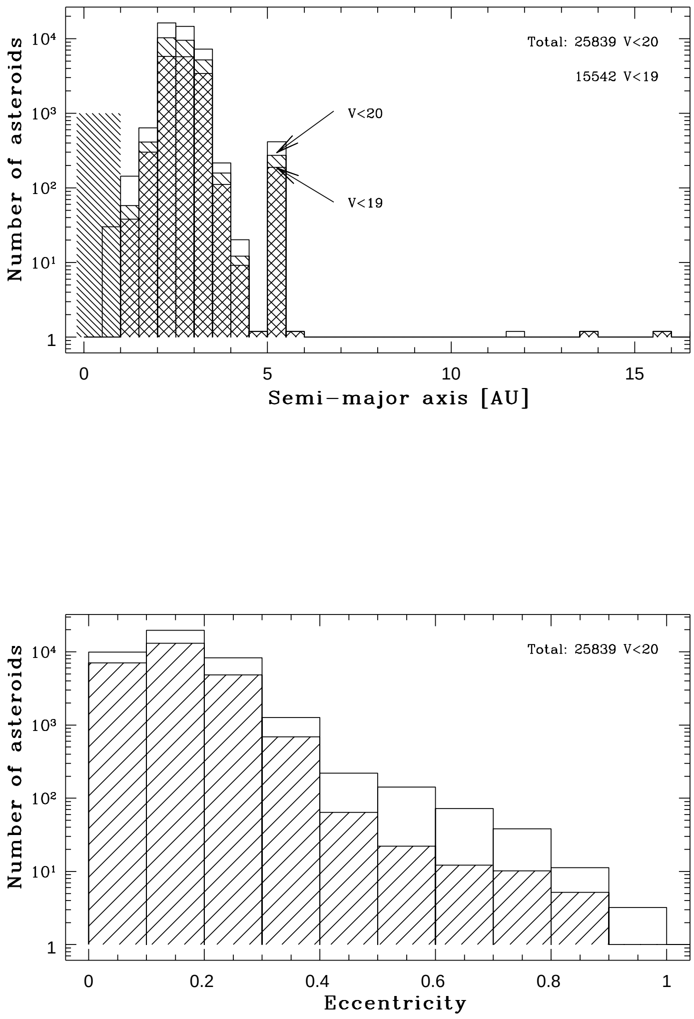

Figure 9: *Histograms – in logarithmic scale – of the observable asteroids (shaded) and the actually cataloged asteroids (Bowell et al. 1994). The shaded box at the left of the upper panel reminds the imposed limit on the semi-major axis ($r \leq 1$). Limiting magnitudes are calculated for observations occuring at the quadrature.*

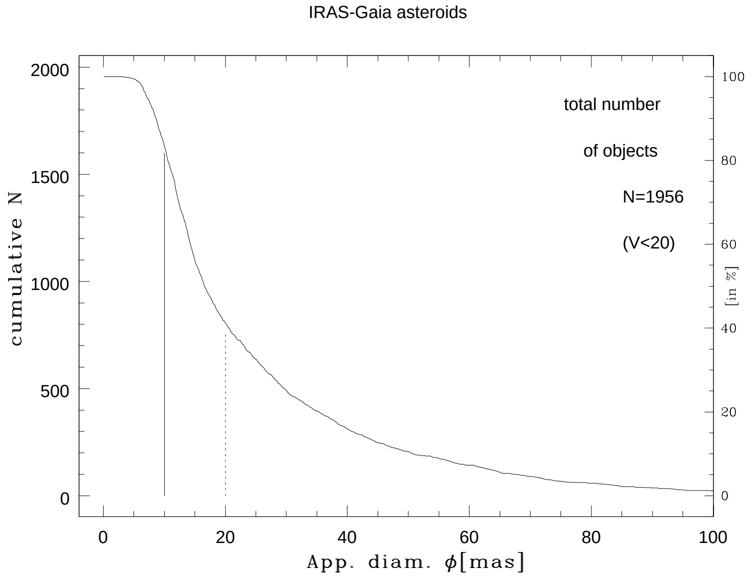

Figure 10: *Cumulative distribution versus apparent diameter of the number of* IRAS *asteroids brighter than $V = 20$ at quadrature.*

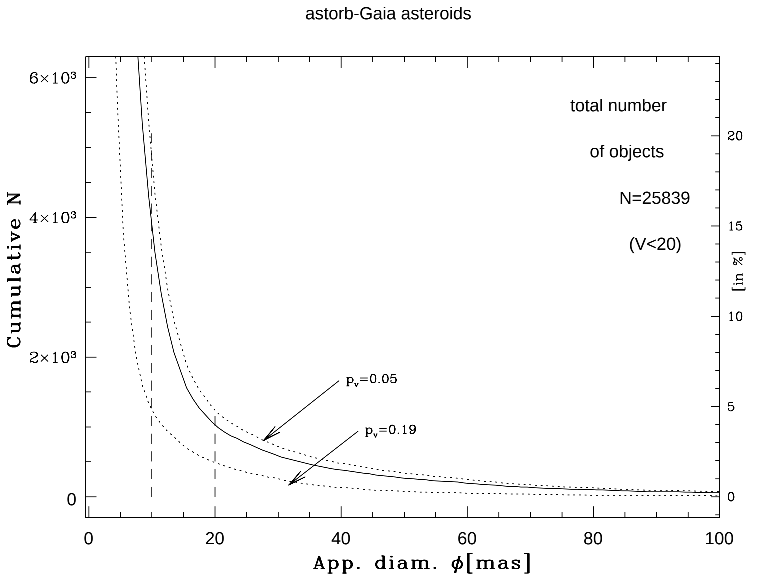

Figure 11: *Cumulative distribution versus apparent diameter of the number of Bowell's catalogue asteroids brighter than V=20 at quadrature versus apparent diameter. The upper and lower dotted curves correspond to objects with an albedo of 0.05 and 0.19 respectively. The filled line yields the cumulative distribution assuming that the population is homogeneous with 75% of dark ($p_{\mathrm{v}} = 0.05$) and 25% of moderate albedo ($p_{\mathrm{v}} = 0.19$) objects.*

10 Number of resolved asteroids

Number of resolved asteroids, at a $3\,\sigma$ level over a CCD or a FOV transit, are given in Table 6. Numbers are given, for the two instruments, for main-belt asteroids, taking into account the variation with magnitude of the precision of the measurement, the limb-darkening, the expected average albedo, and considering a total of 20 s integration time for the whole FOV crossing. Theoretical limits for a uniformly bright object are reminded. Because Trojans are farther from the sun and hence fainter, they will be resolved if they have slightly larger diameters. Number of resolved Trojans are given in Table 7.

If we assume that C-type asteroids (i.e. albedo ranging from 0.03 to 0.09) constitutes 75% of the main-belt population, and the other 25% (S- and M-type with albedo ranging from 0.1 to 0.22) are of larger albedo $p_{\rm v} \sim 0.2$, and hence of smaller angular size at a given magnitude, we find from Table 5 that approximately 1 900 asteroids would be resolved with the interferometer, while with the monolithic telescope, the number of possibly resolved object is 1 300. It is stressed that neither the variation with heliocentric distance for the different taxonomic groups (Gradie & Tedesco 1982), nor the presence of other classes were considered. The Gaia interferometer would hence resolve some 50% more objects than the mono-pupil instrument. One can also note that the power resolution on a single CCD transit yields the number of asteroids that can be considered as point-like sources for the astrometry and the related estimated precisions. For the Trojans, we have assumed that all objects are of low albedo $p_{\rm v} \sim 0.05$. It is reminded that the catalogue is not complete up to magnitude 20, hence more objects would be detected but unlikely resolved. Assuming the catalogue to be complete up to magnitude 17, and all objects of same low albedo 0.05 and at the same distance of 3 AU from the sun, we find that this correponds to a catalogue completeness up to an apparent diameter of 35 mas. Since the resolution power on a FOV transit time scale is close to this value, and under the hypothesis of a catalogue completeness at $V = 17$, the number of resolved objects should not vary significantly (i.e. newly detected unknown objects fainter than $V > 17$ would anyway not be resolved). Thus the numbers of asteroids resolved on a FOV time-scale given here may be considered to be rather realistic.

For the IRAS objects we have made no assumption on the albedo since the magnitude and apparent size are known independently. Assuming again a small darkening of the limb, we find that approximately 1 300 IRAS objects would be resolved with the interferometer, while 1 000 IRAS objects would be resolved with the monolithic telescope. The Gaia interferometer would thus be more advantageous for providing new size determinations.

10.1 Diameter or shape determination

Determination of the length of the cord along the highest resolution direction will be possible over a single transit because the shape of a given asteroid is almost constant over such a time scale. For sake of brevity, we make no

Table 5: *Number of asteroids outside the earth orbit (over a total of 25 800, i.e. $V < 20$) larger than a given apparent size ϕ as a function of albedo p_{v}. A fainter limiting magnitude $V < 19$ would only change the counts for objects smaller than 8 mas. A larger table is provided on the web URL* `http://www.to.astro.it/UserHomeP/hestro/Gaia/tab_resol.dat`

ϕ [mas]$\backslash p_{\mathrm{v}}$	0.05	0.1	0.15	0.2	0.25	0.3	0.35
>4	23057	15277	10948	8435	6757	5582	4717
6	13926	7546	4934	3579	2775	2301	1938
8	8435	4097	2578	1891	1548	1330	1181
10	5376	2484	1651	1290	1091	981	888
12	3579	1702	1219	1010	872	769	677
14	2523	1318	995	815	693	617	545
16	1891	1075	839	672	568	503	452
18	1534	931	697	566	479	425	373
20	1290	797	605	484	414	359	314
22	1119	698	522	425	357	312	274
24	1010	624	462	370	312	266	217

distinction between this length and the apparent diameter ϕ. The precision of the determination is given by:

$$\sigma_\phi(\phi, V) = -\frac{d\mathcal{V}}{d\phi}(\phi)\ \sigma_{\mathcal{V}}(V) + O\left(\sigma_{\mathcal{V}}\right) \tag{17}$$

where the precision of the 'visibility' measurement $\sigma_{\mathcal{V}}$ is given by Eq. (14). The derivative of the visibility depends on the retained option, for the interferometer we have $\mathcal{V}'(\phi) \sim -2\,\mathrm{J}_2(x)/\phi$, where $x = \pi\phi B/\lambda$. For the mono-pupil $\mathcal{V}'(\phi) \sim 7.8\,10^{-5}\,\phi$. For each case, calculation of the derivatives is done by considering a uniformly bright object. Results are shown in Fig. 12. Not surprisingly the interferometer yields better results for small diameters, the resolution power determined above is in fact directly related to this aspect. On the other hand diameter determination is more precise with the monolithic option for objects larger than 60 mas. The relation $\sigma_\phi = f(\sigma_{\mathcal{V}})$ is no more linear for small (i.e. faint) asteroids, and Eq. (17) should be expanded to higher orders for $\phi \lesssim 15 - 20$ mas. For the same reason the precision σ_ϕ given in Fig. 12 is overestimated for an object whose apparent diameter is close to the resolution power. Moreover the distribution of the diameter estimator is no more normal in this case (see Fig. 13). For instance in the case of the bi-pupil instrument and a $p_{\mathrm{v}} = .05$ asteroid, simulations show that the distribution of ϕ is normal when $\phi \geq 19$ mas; value to compare to the power resolution of $\phi = 14$ mas in Table 6.

Over a FOV transit time-scale, the interferometer would enable the diameter determination of a $\phi = 20$ mas ($p_{\mathrm{v}} = .05$) or a $\phi = 15$ mas ($p_{\mathrm{v}} = .2$) asteroid with a relative precision of approximately 6%. Such a precision is reached with the monolithic option for a $\phi = 25$ mas ($p_{\mathrm{v}} = .05$) or a $\phi = 20$ mas ($p_{\mathrm{v}} = .2$)

Table 6: *Resolution power and number of resolved main-belt asteroids for the interferometer and the monolithic telescope, over either a single* CCD *(left table) or a* FOV *transit (right table). The percentage with respect to detectable objects exterior to the earth's orbit ($V < 19$ or 20, and $a \geq 1$) is given in brackets. For the interferometer, numbers are given considering a filter with a 200 nm* FWMH. *In the case of the mono-pupil telescope, numbers are given for the 300–1 200 nm broad-band G filter. Asteroids are supposed to be limb-darkened following Minnaert's law with a constant parameter $k(\lambda, \alpha) = k = 0.65$. Since the albedo is unknown for the* `astorb` *data set, the population is considered to consist of 75% of C-type asteroids ($p_v = 0.05$) and 25% of S- or M-type asteroids ($p_v = 0.2$).*

	Bi-pupil	Mono-pupil
λ [nm]	750	300-1 200
CCD transit		
$p_v = 0.01$		
ϕ_{UD} [mas]	31	37
ϕ_{min} [mas]	32.5	39
$p_v = 0.03$		
ϕ_{UD} [mas]	26	31
ϕ_{min} [mas]	27	32.5
$p_v = 0.05$		
ϕ_{UD} [mas]	23	28
ϕ_{min} [mas]	24	29
$p_v = 0.20$		
ϕ_{UD} [mas]	18	23
ϕ_{min} [mas]	19	24
IRAS	713 (37.4)	550 (29.0)
`astorb`	850 (5.6)	660 (2.6)

	Bi-pupil	Mono-pupil
	750	300-1 200
FOV transit		
$p_v = 0.01$		
ϕ_{UD} [mas]	18	23
ϕ_{min} [mas]	19	24
$p_v = 0.03$		
ϕ_{UD} [mas]	15	19
ϕ_{min} [mas]	16	20
$p_v = 0.05$		
ϕ_{UD} [mas]	14	17
ϕ_{min} [mas]	15	18
$p_v = 0.20$		
ϕ_{UD} [mas]	11	14
ϕ_{min} [mas]	12	15
IRAS	1 290 (67.5)	1 000 (52.3)
`astorb`	1 810 (11.8)	1 270 (5.0)

asteroid. Figure 12 should be used for larger diameters only.

Such an analysis can easily be extended to the case of a star. Here only the apparent magnitude is to consider. At $V = 15$ a star larger than approximately 8 mas would be resolved with the interferometer on a transit time scale (20 s observing time). Diameter determination over a transit time-scale would be better than 1% only for bright stars (see Fig. 14). A precision of 1% for a $V = 15$ star can however be reached by combining the data over the 5 years mission.

Asteroids are not spherical. Analysis of the photometry, or adaptive optics as well as HST observations in interferometric mode (FGS3) are well interpreted by assuming a tri-axial ellipsoid. It has also been possible to determine flattening of stars from large-baseline interferometric observations. For a theoretical interferometer operating in monochromatic light and with $B \gg D$, there is no influence of the disk flattening (ellipsoidal shape) on the signal over a transit (see Sect. S:integral). With the Gaia interferometer this influence is negligible for $0 < \zeta = b/a \lesssim 3$ (i.e. for realistic 'flattening'). Thus for

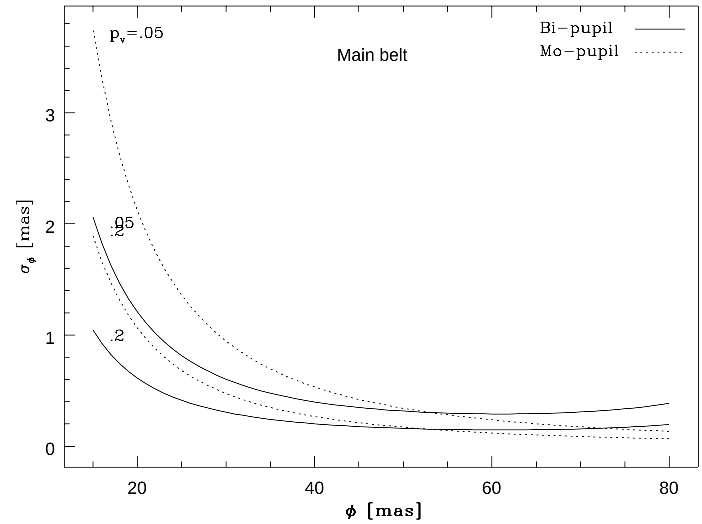

Figure 12: *Precision of the diameter determination for an asteroid over a single* FOV *transit.*

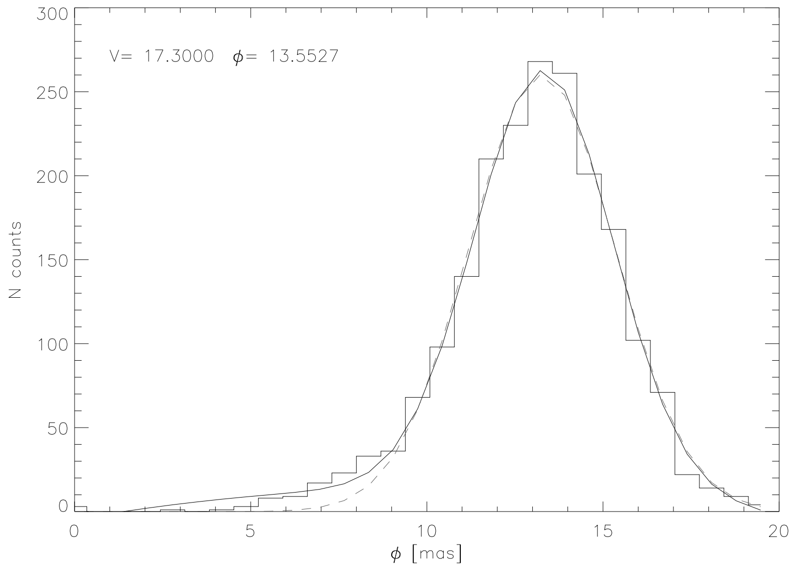

Figure 13: *Dispersion of the diameter estimation for small diameters. The graph is given for an asteroid at the limit of resolution by the interferometer over a* FOV *transit time scale* ($V = 17.3$, $p_{\rm v} = .05$, $\phi \sim 14$ mas)*. The solid line shows an exponential fit combined with a quadratic component, while the dashed curve shows the Gaussian fit.*

Table 7: *Number of resolved Trojans of Jupiter. Similar to Table 6 however all* `astorb` *objects were considered to be of the same low albedo* $p_v = 0.05$.

λ [nm]	Bi-pupil 750	Mono-pupil 300-1 200
CCD transit		
$p_v = 0.01$		
ϕ_{UD} [mas]	36	43
ϕ_{min} [mas]	37.5	45
$p_v = 0.03$		
ϕ_{UD} [mas]	30	36
ϕ_{min} [mas]	31.5	37.5
$p_v = 0.05$		
ϕ_{UD} [mas]	27	32
ϕ_{min} [mas]	28	33.5
$p_v = 0.20$		
ϕ_{UD} [mas]	21	26
ϕ_{min} [mas]	22	27
IRAS	15 (33.3)	6 (13.3)
`astorb`	20 (10.4)	10 (3.6)

	Bi-pupil 750	Mono-pupil 300-1 200
FOV transit		
$p_v = 0.01$		
ϕ_{UD} [mas]	21	26
ϕ_{min} [mas]	22	27
$p_v = 0.03$		
ϕ_{UD} [mas]	18	22
ϕ_{min} [mas]	19	23
$p_v = 0.05$		
ϕ_{UD} [mas]	16	20
ϕ_{min} [mas]	17	21
$p_v = 0.20$		
ϕ_{UD} [mas]	13	16
ϕ_{min} [mas]	14	17
IRAS	43 (95.6)	35 (77.8)
`astorb`	90 (46.9)	60 (21.7)

each transit one will determine an equivalent diameter considering the object is spherical. The flattening may become noticeable when one analyses the measures over the whole mission. The visibility of the fringes, or the FWMH for the mono-pupil will vary not only with the geocentric distance (actually the distance w.r.t. the Gaia satellite) but also with the aspect, obliquity and rotation angles of an asteroid, and the scanning direction. Theoretically one should determine the distance to the satellite, one scaling parameter, the limb darkening, the ratios $a : b : c$, the coordinates of the pole of the asteroid, the rotation period and the origin meridian of this rotation. However the bi-pupil Gaia observations will not be optimal to derive the shape of any asteroid from such data but will either provide a test from existing model or some limiting values. The mono-pupil Gaia telescope will provide a two-dimensional image – but with very different resolutions – over a single transit. Thus Gaia will preferably provide a mean diameter – as was the case with IRAS survey – by combining the data gathered over the whole mission duration, and eventually indication of elongated tri-axial ellipsoids.

10.2 Asteroids binaries

Gaia will also enable separation of stellar binaries or multiple systems. Of particular interest is the availability of Gaia to detect close asteroids binaries. A binary asteroid is more likely composed of two similar bodies of approximately the same size and magnitude, and gravitating closely around each

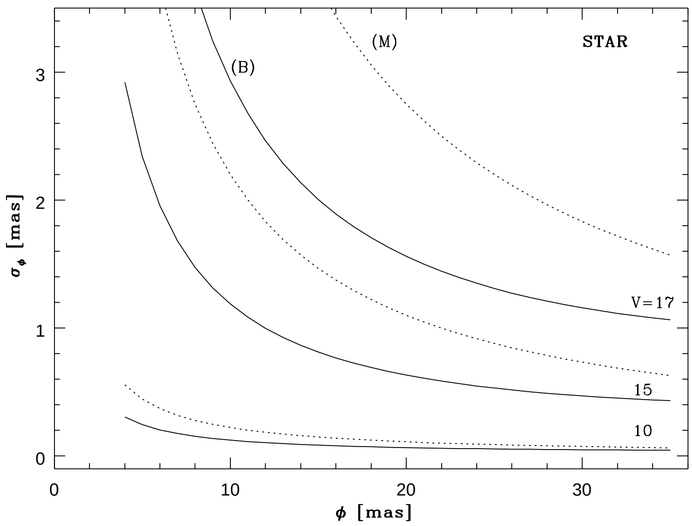

Figure 14: *Precision of the diameter determination for a star over a single* FOV *transit and for different apparent magnitudes V. Solid curves given for the interferometer (B), and dotted curves for the monolithic telescope (M).*

other. One finds that a contact binary formed of equally bright objects larger than approximately 60 mas would be resolved with the monolithic telescope. For smaller objects, and given the sampling by the CCD, the binary system would hardly yield a signal different from that of a single resolved object. The interferometer on the other hand may be a better instrument for such a purpose. It could detect contact binaries of smaller size up to magnitude $V \lesssim 15$ although amgiguous cases remain. Figure 15 shows the Fourier transform of a contact binary system composed of two identically large and bright spherical bodies. It appears from the analysis of the higher frequencies that it should be possible to reveal – on a transit time scale – the binary nature from a single resolved object.

11 Comparison

With a fainter limiting magnitude, the mono-pupil telescope will enable to determine the position of a larger number of (small) known asteroids (66% more than the interferometer). The resolution power of the interferometer is on the other hand higher, enabling diameter determination of about 50% more objects than the monolithic telescope. The interferometer will also be able to test the IRAS determination of diameters for 30% more objects than the monolithic telescope. Diameter determination is more precise with the interferometer for objects smaller than $\phi \leq 60$ mas; for larger objects the mono-

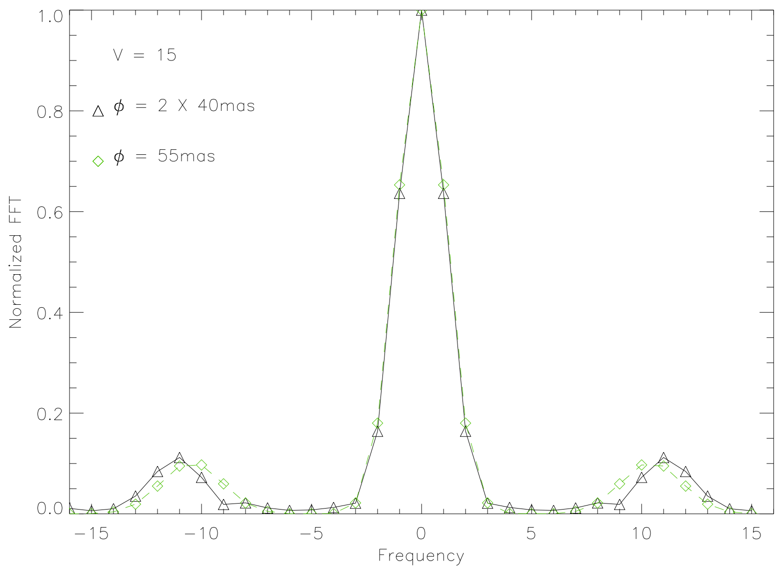

Figure 15: *Fourier transform of the interferometeric signals from a binary system and a single extended object.*

lithic telescope would yield slightly better results. Bright asteroids ($p_v \sim 0.2$) larger than approximately 20 km at 3 AU or 35 km at 5 AU would be resolved by the mono-pupil. With the bi-pupil corresponding sizes are 15 km at 3 AU or 30 km at 5 AU. Very dark asteroids ($p_v \sim 0.01$) are resolved only if they are larger than approximately 30 km at 3 AU or 50 km at 5 AU. However the precision of the diameter determination is, by definition, close to 33% at the resolution limit. Diameter determination of Trojans at a few percent level objects becomes possible when they are larger than roughly 50 km with the interferometer, and 60 km with the monolithic telescope.

Table 8: *Comparison of the mono- and bi-pupil options.*

	Bi-pupil	Mono-pupil
Number of detected objects	-	+
Astrometry degradation	-	+
Number of resolved objects	+	-
Diameter determination	+	-
Binares detection	+	-
IRAS diameters	+	+

12 Conclusion

For both the MMS and ALS solutions, hundreds of asteroids would be resolved yielding a possible determination of their diameter. However a limiting resolution of approximately 20 mas would be of lower interest with respect to the number of objects whose diameter could be provided within a few percent over a single FOV transit. As long as the diameter determination for an appreciable number of asteroids is concerned, in particular for testing the model-dependent IR diameters from the IRAS survey, the 2.45 m baseline interferometer with a $V < 19$ limiting magnitude and the $1.7 \times 0.7\,\mathrm{m}^2$ monolithic telescope are suitable. Another important output is the determination of the density of those objects for which Gaia would provide the mass. The accuracy of the diameter determination will rely on the signal-to-noise ratio and to a smaller extent on the object's size. Determination of the order of the percent in relative precision should be achievable for a large proportion of the IRAS objects. Both instruments can provide sufficient data for scaling IRAS-type determinations. The interferometer would be more suitable than the monolithic telescope for the detection of asteroids binaries. On the other hand, due to its fainter limiting magnitude, the monolithic option would provide astrometry and photometry for a larger number of asteroids.

Since the contrast of the fringes is lower with increasing apparent diameter, the astrometry will be of poorer quality for the resolved objects in the interferometric mode (Gai et al. 1998a, 1998b). On the other hand, this loss of precision will be smaller with the monolithic option, and for a smaller number of objects. One has however to keep in mind that it would be unrealistic to provide the position of say a few 0.1 arcsec large asteroid with a 0.1 mas precision since one could hardly link the actual observed position to the usual photocentre or center of mass. In this case the position could still be given with fairly good precision from the analysis of the Airy pattern (see note in Sect. A.4) because the signal-to-noise ratio is high (large asteroids are typically bright objects).

Regarding this aspect, it is interesting to see whether there is a loss of essential astrometric information by enhancing the resolution power. With respect to the determination of mass of asteroids, the astrometry of the larger asteroids is not particularly useful. With respect to the determination of the parameter β of the parameterized general relativity, one will prefer high precision astrometry of those asteroids of largest eccentricity which is not totally correlated to their size. With respect to the dynamical-kinematical reference frames link, one will prefer point-like objects in order to minimize the – subject to model errors – photocentre displacement due to phase effect. On the other hand, a large number of objects with high precision astrometry (i.e. preferably bright objects) is profitable since the "mean errors decrease with increasing mission length and number of planets observed" (Söderhejlm & Lindegren 1982), see note in Sect. B.1. In conclusion, enhancing slightly the power resolution should not have disastrous effects on the astrometry; it is the limiting magnitude that is of higher importance here.

It is stressed that the numbers derived here concern the achievable resolution on a single transit. Contrarily to an asteroid, the resolution power is enhanced in the case of a typical star (i.e. radially symmetric, no time variation of the diameter, ...) observed 100 to 200 times during the mission. Analysis of the resolution of stars should be done in a future work. Similarly an average diameter for an asteroid can be derived with a better precision by combining the data of all its FOVs transits.

Acknowledgments. *Thanks to F. Mignard for providing the code of the calculation of the* PSFs*, also to A. Doressoundiram for his help on the modeling of asteroid spectra, and to M. Gai for helpful comments and suggestions.*

References

[1] Bowell E., Muinonen, K., Wasserman L.H., 1994, in: ACM 1993, A. Milani, M. Di Martino and A. Cellino (eds.). Kluwer Academic, Dordrecht, p. 477.
`ftp://ftp.lowell.edu/pub/elgb/astorb.dat.gz`

[2] Gai M., Casertano S., Carollo D., Lattanzi M., 1998a, PASP 110, 848.

[3] Gai M., Carollo D., Lattanzi M., 1998b, Interferometric GAIA option on extended and moving targets, Tech. Rep., OATO.

[4] Gradie J., Tedesco E., 1982, Science 216, 1405

[5] Hestroffer D., 1997, A&A 327, 199

[6] Mignard F., 1998a, The GAIA broad-band photometric system. Tech. Rep. SAG_FM_002

[7] Mignard F., 1998b, Optical and pixel blurred PSF of GAIA. Tech. Rep. SAG_FM_005

[8] Söderhjlem S., Lindegren L., 1982, A&AS 110, 156

[9] Tedesco E.F., 1989, in: Asteroids II, R. Binzel, T. Gehrels and M.S. Matthews (eds). The Univ. of Arizona Press.
`http://pdssbn.astro.umd.edu/SBNast/archive/diamalb.tab`

[10] Xu S., Binzel R.P., Burbine T.H., Bus S.J., 1995, Icarus 115, 1
`http://pdssbn.astro.umd.edu/SBNast/archive/smass.tab`

A Notes

A.1 Filters

Adopting a filter centered at a smaller wavelength will not increase dramatically the number of resolved asteroids with the interferometer. Doing so, the gain in the power resolution of the instrument is balanced by the fact that (i) asteroids are fainter in the B band and (ii) the precision of the measure degrades rapidly for small (i.e. faint) objects. Nonetheless the situation for a star would be different because its magnitude is not tied to its size.

A.2 Atens

There are more known Atens than present in the `astorb.dat` data-file, but nonetheless there are less chances that Gaia will observe a given Aten-asteroid during the 5 years mission since observations will occur when an Aten is near its maximal elongation and because Atens are roughly co-rotating with the telescope. Moreover such objects are small (a few kilometers in size) yielding a apparent diameter of roughly 1 to 7 mas at 1 AU. In addition their motion on the sky is high, which will contribute to larger errors during the reduction of the CCD's data. Ability to observe or discover such objects should be the aim of a dedicated study, but for the reasons given above Atens and other NEAs are not of dramatic importance in the present one.

A.3 Eccentricity

Figure 16 shows the cumulative distribution of Bowell's catalogue. With a five years mission duration, Gaia will observed a typical main-belt asteroid over a whole orbital period (see Table 9). Hence the number given here, while considering circular orbits, should correspond to an average number of resolved objects although a highly eccentric asteroid may not be resolved or even detected at each transit in the FOV. Considering that all observations occur when the objects are either at their perihelion or aphelion, we can derive the following bounding limits for the number of detectable objects (i.e. $V < 20$) in `astorb.dat`: 31 500 (perihelion) and 20 200 (aphelion). One can also note that the orbital coverage of a typical Trojan object will be limited. Hence, as was the case for the Hipparcos (main-belt) asteroids, Gaia will not provide the whole set of osculating elements for ephemeris improvement of Trojans while the situation for the Gaia main-belt asteroids should be improved.

A.4 Astrometry of large objects

For objects too large to provide valuable fringes pattern ($\phi \gtrsim \lambda/B$), astrometry can still be derived, as for the monolithic telescope, from the analysis of the Airy pattern or single aperture PSF. The pixel size is a parameter to

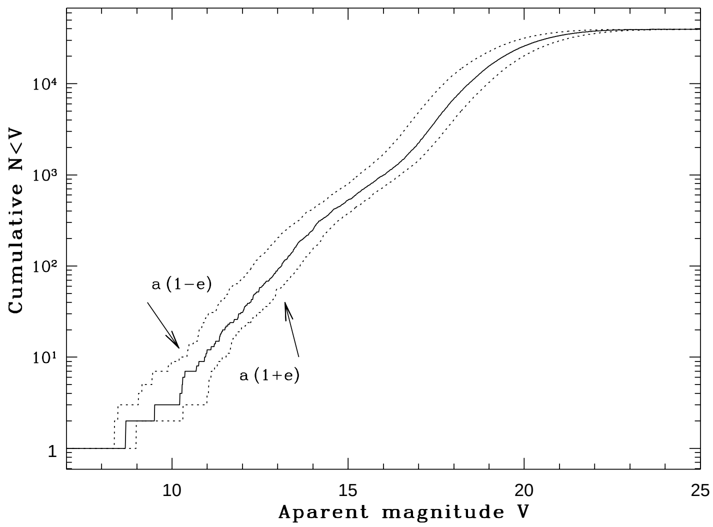

Figure 16: *Cumulative distribution – in logarithmic scale – versus apparent magnitude for Bowell's catalogue asteroids. The upper and lower dotted curves correspond to observations at perihelion and aphelion respectively.*

Table 9: *Orbital period in year vs. semi-major axis.*

a [AU]	1	2	3	4	5	6
$1/n$ [yr]	1	2.8	5.2	8	11.2	14.7

consider to estimate the precision one can reach. However, at a given acceptable sampling rate, the signal-to noise ratio is of main importance, which in any case will be important because the largest objects are generally the brightest ones. As a consequence, astrometry of such objects could still be of valuable quality with both options. For instance, Gai et al. (1998a) estimate the astrometric dispersion to 1.4 mas for a V=12.5 object and a 6 mas pixel size when the visibility is low, value to compare to 0.2 mas for a maximal visibility of 100%. One will have to consider possible blooming effect, these are however strongly dependent on the CCD's well capacity and size, and the time integration over one chip operating in TDI mode.

B Future work

B.1 Dynamical reference frame

The work of Söderhejlm & Lindegren (1982) was dedicated to simulation of Hipparcos observations and hence they considered only a small number of objects (up to 25). Due to hysteresis phenomena, the precision σ of the planetary-extragalactic reference frames link should converge asymptotically to a given positive limit l with the (large) number of objects N observe with Gaia:

$$\sigma \to 1/\sqrt{N} + l, \ N \gg 1$$

Hence, given a certain number of objects N_o (still to define), the precision of the determination of the various parameters of the problem will not be significantly improved by degrading the resolution power of the telescope. One could consider for instance that all the objects smaller than approximately 40 mas would yield valuable astrometry; in this case astrometry of only a few percent of objects would be degraded. A more careful simulation of the precision of the reference frames link should be done in a next analysis.

B.2 Object's motion

One may want to model the motion during the ~ 20 s transit across the $0\overset{\circ}{.}7$ FOV to increase the accuracy of the astrometry and photometry as was the case for Hipparcos. One should be able to determine this motion with a sufficient precision to correct for the blurring effect in the various CCDs acquisition either a posteriori, or in real time by a proper clocking of the CCD. Hence, producing sufficiently accurate orbits of the detected asteroids from ground-based observations campaign would be profitable. Moreover good ephemerides are needed for the knowledge of the asteroid's distance to the Gaia satellite which is needed for the reduction to conventional astrometric positions instead of apparent positions w.r.t. the artificial satellite.

C Numerical codes

C.1 Integration for a resolved object

Assuming that the PSF and the brightness distribution of the source are almost constant in the y direction (i.e. the direction perpendicular to the scan), $P(x,y) = P(x,-)$ and $I(u,v) = I(u,-)$, we find that the image of a disk $\mathcal{D}$ is identical to the image of an ellipse $\mathcal{E}$ scanned along a direction of position angle γ (see Fig. 17):

$$\frac{\int\int_{\mathcal{D}} I(u,v)P(x-u,y-v)\,du\,dv}{\int\int_{\mathcal{D}} I(u,v)\,du\,dv} = \frac{\int\int_{\mathcal{E}} I(u,v)P(x-u,y-v)\,du\,dv}{\int\int_{\mathcal{E}} I(u,v)\,du\,dv}$$

$$\int\int_{\mathcal{D}} I(u,v)P(x-u,y-v) = 2\int_{u=-1}^{1} I(u,-)P(x-u,-)\left(\int_{v=0}^{\sqrt{1-u^2}} dv\right) du$$

$$\begin{aligned}
&= \zeta^{-1}\int_{-1}^{1} I(u,-)P(x-u,-)\int_{0}^{2\,\zeta\sqrt{1-u^2}} dv\,du \\
&= (2\,\zeta)^{-1}\int_{-1}^{1} I(u,-)P(x-u,-)\int_{-2\,\zeta\sqrt{1-u^2}}^{2\,\zeta\sqrt{1-u^2}} dv\,du \\
&= (2\,\zeta)^{-1}\int_{-1}^{1} I(u,-)P(x-u,-)\int_{-(\zeta^2-1)\sin(2\gamma)\,u-2\,\zeta\sqrt{1-u^2}}^{-(\zeta^2-1)\sin(2\gamma)\,u+2\,\zeta\sqrt{1-u^2}} dv\,du \\
&= \tau^2\zeta^{-1}\int_{-1}^{1} I(u,-)P(x-u,-)\int_{\left(-(\zeta^2-1)\sin(2\gamma)\,u-2\,\zeta\sqrt{1-u^2}\right)/(2\tau^2)}^{\left(-(\zeta^2-1)\sin(2\gamma)\,u+2\,\zeta\sqrt{1-u^2}\right)/(2\tau^2)} dv\,du
\end{aligned}$$

which is equal to $\pi\tau^2\zeta^{-1}\int\int_{\mathcal{E}} I(u,-)P(x-u,-)\,du\,dv$, i.e. the integral over the ellipse of equation[2]:

$$(\mathcal{E}) : r^2\cos^2(\theta-\gamma) + \frac{r^2\sin^2(\theta-\gamma)}{\zeta^2} = \tau^{-2}$$

This ellipse has a flattening ζ, a semi-major axis $a = \tau^{-1} = (\cos^2\gamma + \zeta^2\sin^{\gamma})^{-1/2}$ and a position angle γ wrt the scanning direction. With $u = r\cos\theta$ and $v = r\sin\theta$, we find after some calculation the result in cartesian coordinates for $u \in [-1;\,1]$:

$$v(u) = \frac{-(\zeta^2-1)\sin(2\gamma)\,u \pm 2\,\zeta\sqrt{1-u^2}}{2\tau^2}$$

In the real case (diffraction and limb-darkening in the y direction) the difference between both PSFs is small (less than 2% for an object of size

[2]It is stressed that the degenerate case $\zeta = 0$ does not correspond to the image of a strip of uniform brightness distribution

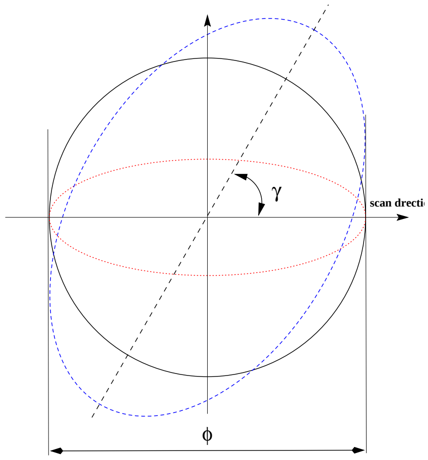

Figure 17: *All elliptical shapes of along-scan length ϕ and of uniform brightness distributions yield the same along-scan* PSF.

$\phi \lesssim 110$ mas with the bi-pupil and $\phi \lesssim 60$ mas for the mono-pupil) and can be neglected. Also the assumption $P(x,y) = P(x,-)$ is valid for a restricted range of 'flattening', we find that for realistic values of $\zeta < 3$ the approximation is still acceptable.

The brightness distribution with Minnaert's law for a flattened disk is given at full phase by:

$$I(u,v) = (1 - u^2 - v^2/\zeta^2)^{(k-1/2)}$$

The brightness distribution for a flattened disk when there is a phase is given by:

$$\begin{array}{lclcl} I(u,v) & = & (1 - u^2 - v^2/\zeta^2)^{(k-1/2)} & \text{if} & u^2/\cos^2\alpha + v^2/\zeta^2 \leq 1 \text{ or } u > 0 \\ I(u,v) & = & 0 & \text{if} & u^2/\cos^2\alpha + v^2/\zeta^2 > 1 \text{ and } u > 0 \end{array}$$

C.2 Calculation of the PSF

The FORTRAN code `psfR.for` calculates the PSF for a resolved object not larger in apparent size than $\phi \lesssim 110$ mas. For larger objects, the size of the frame should be enlarged and the various step sizes in the numerical calculation should be changed to ensure sufficient accuracy. Hence the code can be adapted to the observations of larger objects but would necessitate longer integration time. Since we are interested in the resolution power of the instrument, we restrict ourself to the case of medium-size objects. Compilation of the code and subroutines is done by invoking under Unix the `MakepsfR` makefile. The necessary inputs parameter are given in the file `psfR.in` shown in Table 10. First the static PSF is calculated for a point-like source of given spectral type and magnitude $V = 15$ with a step size of $0.5\,\mu$m, next this is used for integration over the resolved object shape and orientation, and finally the two-dimensional signal in the focal plane from the resolved object obtained in TDI mode is calculated for each logical pixel. Usually the image in the focal plane consists of a 256×256 nodes frame for a total size of $64 \times 64\,\mu\mathrm{m}^2$. Depending on the options used (M or B), output files of the images for the static and TDI mode are:

- `psfRB.dat`: Bi-pupil two-dimensional static PSF
- `psfRBc.dat`: Bi-pupil along-scan one-dimensional static PSF
- `psfRB_TDI.dat`: Bi-pupil two-dimensional TDI-mode PSF
- `psfRB_TDIc.dat`: Bi-pupil along-scan one-dimensional TDI-mode PSF
- `psfRM.dat`: Mono-pupil two-dimensional static PSF
- `psfRMc.dat`: Mono-pupil along-scan one-dimensional static PSF
- `psfRM_TDI.dat`: Mono-pupil two-dimensional TDI-mode PSF
- `psfRM_TDIc.dat`: Mono-pupil along-scan one-dimensional TDI-mode PSF

The one-line header of the one-dimensional PSF files gives the number of records (points), the step size in microns and the apparent size of the source in mas. For each record are given the along-scan position in number of logical pixel, the position in microns and the intensity in $e^-/\mu\mathrm{m}^2/s$. The one-line header of the two-dimensional TDI-mode PSF files gives the number of records, the number of points per record, the focal length, the baseline length for the bi-pupil (or the pupil length for the mono-pupil), the pupil diameter for the bi-pupil (or the pupil width for the mono-pupil), the optical transmittance, the Strehl ratio, the reference wavelength for the Strehl correction, the spectral type of the source, the V magnitude, the pixel width, the pixel height, the absorption, the filter code, the source velocity (or TDI drift), the along-scan step-size in microns, the cross-scan step-size in microns, the apparent size of the source in mas, the limb-darkening parameter, the flattening coefficient, the solar phase angle, and the position angle of the major axis . The header for the static image is identical excepted for the pixel size data which are not given. Following the two-dimensional intensity frame in $e^-/\mu\mathrm{m}^2/s$ is given.

C.3 Resolution power

The IDL code `plotpsf.pro` calculates for a given magnitude and apparent size of the source the re-scaled PSF, the empirical fits, the Fourier transforms and the visibilities estimations. For simulation of the precision of the visibility measurement, a loop of 200 iteration is performed for the calculation of the visibility. This yields the variation with magnitude of the precision of the visibility, and the variation with the source's apparent size of the visibility. From these and given the asteroid's albedo, the $3\,\sigma$ level for the resolution power can be determined on a CCD or FOV transit time scale.

Table 10: *Input parameters of the code* `psfR`.

Parameter	Variable	default value
Option	PUPIL	–
Focal length (M)	F_M	50 m
Focal length (B)	F_B	40 m
Baseline (B)	B	2.45 m
Pupil diam. (M)	D	0.6 m
Pupil x (M)	XPUP	1.7 m
Pupil y (M)	YPUP	0.7 m
Optical transmittance	OPT	0.9
Strehl ratio	STREHL	0.8
Strehl wavelength	WAVE_0	500 nm
Scan velocity x	OMEGAX	120″/s
Scan velocity y	OMEGAY	0″/s
Asteroid velocity	DRIFT	0″/s
Pixel width (M)	DXSI_M	9 μm
Pixel height (M)	DETA_M	27 μm
Pixel width (B)	DXSI_B	4 μm
Pixel height (B)	DETA_B	50 μm
Spectral type	ISPEC	28
Filter (M)	NUMFI_M	0
Filter (B)	NUMFI_B	6
Magnitude V	XMAG	15
Absorption	AV	0
Along scan size	XPHI	– mas
Limb darkening	XLD	0.5
Flatening	XFLA	1.
Phase angle	XPHAZ	0. deg
Position angle	XPOS	0. deg